

Robust Machine Learning Framework for Reliable Discovery of High-Performance Half-Heusler Thermoelectrics

Shoeb Athar, Adrien Mecibah, and Philippe Jund*

ICGM, Univ Montpellier, CNRS, ENSCM, 34293 Montpellier, France

E-mail: philippe.jund@umontpellier.fr

Abstract

Machine learning (ML) can facilitate efficient thermoelectric (TE) material discovery essential to address the environmental crisis. However, ML models often suffer from poor experimental generalizability despite high metrics. This study presents a robust workflow, applied to the half-Heusler (hH) structural prototype, for figure of merit (zT) prediction, to improve the generalizability of ML models. To resolve challenges in dataset handling and feature filtering, we first introduce a rigorous PCA-based splitting method that ensures training and test sets are unbiased and representative of the full chemical space. We then integrate Bayesian hyperparameter optimization with k-best feature filtering across three architectures—Random Forest, XGBoost, and Neural Networks—while employing SISSO symbolic regression for physical insight and comparison. Using SHAP and SISSO analysis, we identify A-site dopant concentration ($x_{A'}$), and A-site Heat of Vaporization (HVA) as the primary drivers of zT besides Temperature (T). Finally, a high-throughput screening of approximately 6.6×10^8 potential compositions, filtered by stability constraints, yielded several novel high- zT candidates. Breaking from the traditional focus of improving test $RMSE/R^2$ values

of the models, this work shifts the attention on establishing the test set a true proxy for model generalizability and strengthening the often neglected modules of the existing ML workflows for the data-driven design of next-generation thermoelectric materials.

Keywords: *machine learning, principal component analysis for train/test split, feature filtering, high-throughput screening, thermoelectric materials, half-Heuslers*

Introduction

The development of efficient thermoelectric (TE) materials which can produce electricity directly from heat through the Seebeck effect is an urgent need in the context of the present environmental crisis. The performance of a TE material is gauged by the dimensionless figure of merit zT given by¹ $zT = S^2\sigma T/\kappa$ (where S is the Seebeck coefficient (V.K^{-1}), T is the working temperature (K), σ is the electrical conductivity (S.m^{-1}), and κ is the thermal conductivity ($\text{W.m}^{-1}\text{.K}^{-1}$)). A good TE material, therefore, must have high electrical conductivity and Seebeck coefficient – lumped together as $S^2\sigma$ or the TE power factor – as well as low thermal conductivity. Identifying such materials is a highly challenging task because of the intricate interplay between these properties. Significant research into efficient TE materials has yet to yield widespread commercial success, hindered by the toxicity and scarcity of constituent elements (e.g., Pb, Te, and Ge) and the susceptibility of TE modules to mechanical failure under fluctuating thermal and mechanical stresses^{2,3}. Steady progress in artificial intelligence has opened new horizons in the accelerated discovery and design of functional materials⁴ versus time-consuming and / or trial-and-error-based experimental or density functional theory (DFT) pathways. Machine learning (ML) has emerged as a powerful technique to design and screen materials with required functionalities⁴. TE materials have also recently benefited from the composition design assisted by ML⁵. Several studies have demonstrated that ML can not only be used to predict individual transport properties but also complex properties like the power factor or the zT for various materials⁶. However, even with advances in ML techniques, the discovery and experimental synthesis of new high

performance TE materials through an exhaustive search for vast compositional spaces is challenging⁷ due to one or more of the following reasons: lack of large curated datasets; poor generalizability of ML models; the structural diversity and complexity of TE materials;⁸ and structural/phase stability of the predicted materials.

We have addressed the issue of dataset size and curation in our previous work.⁹ To mitigate the problems associated with structural diversity and complexity of TE materials, we restrict the present study on a specific structural prototype: half-Heusler (hH) TE materials. While the ideal solution is the inclusion of relevant structural and crystallographic features, the data-diversity in the existing datasets⁹ with respect to different structural prototypes is not sufficient to allow for such an approach. The high-throughput synthesis approach of phase- and structurally-stable ML predicted materials will be the subject of our next work. In this work, we focus on the causes of poor generalizability of ML-models for TE materials and the solutions thereof.

A typical machine learning workflow entails the following modules: dataset construction and curation, data pre-processing, feature selection, model construction and evaluation, model interpretation, and high-throughput screening (HTS). Generalizability of an ML-model particularly depends on the first four components. While several studies have reported sophisticated workflows for ML-application for TE materials^{10–14}, some key challenges associated with dataset pre-processing (splitting training/test data) and feature selection process have not been addressed yet. The first challenge concerns the splitting of training and test data. Statistical bounds like Hoeffding and Vapnik-Chervonenkis (VC)¹⁵ require that training and test distribution must be the same i.e. they must be generated from the same distribution of the input space. According to Abu-Mostafa et al. 2012: “If the data is (inadvertently) sampled in a biased way, learning will produce a similarly biased outcome.” If the training data is generated with exclusion of a certain part of the input space, or chemical space, the final model trained with it may not generalize¹⁵. Conversely, the test data obtained from only a small part of the chemical space, may not suffice as a

true proxy to gauge the out-of-sample error. We have explained this in detail in our another work⁶ . Therefore, a “fair” split of the Train/Test data, based on the chemical space of the dataset, is extremely crucial. Here, it is important to note the hierarchical structure - based on materials (element dependent), compositions (concentration dependent), and data points (temperature dependent)⁹ - of the experimental TE datasets. A train/test split based on the lower levels of the hierarchy (concentration or temperature dependencies) can give misleading test scores as they would only reflect the interpolation ability of the model with respect to concentrations or measurement temperatures. While researchers are cautious in splitting the train/test subsets based on the top hierarchy of the materials,^{4,10} to the best of our knowledge there is no reported standard method to fairly split the dataset based on the equivalent representation of chemical space along with the target property for TE materials(zT). Tranås et al. (2021) have proposed a principal component analysis (PCA) based distribution of train and test data points¹⁶ . However, this study was for a DFT-based non-hierarchical dataset and still lacked consideration for the other possible train/test distributions equivalent in chemical space but different in the ease of model fitting. Both the input space and target property distribution of the train/test data determines the ease of model fitting. However, selecting the train-test split after observing the test data may constitute data snooping.¹⁵ .

The second challenge is related to the feature selection method. Derived from several interdependent intrinsic bulk physical properties (S , σ , and κ), the TE figure-of-merit depends on the complex interplay of physical, structural, and electronic properties of constituent elements as well as bulk structure. Selecting a relevant and adequate number of those properties as primary features is essential to avoid under-representation of zT in ML-training. Conversely, incorporation of a large number of irrelevant and redundant features may not only increase computation time but also result in multicollinearity-caused overfitting¹¹ . Therefore, feature selection methods are crucial to check relevancy and redundancy of features. They help decrease the size of the feature space by detecting and removing highly inter-

correlated features¹⁷ . Current feature filtering methods are broadly classified into three categories viz. filter, wrapper, and embedded methods¹⁸ . Filter method uses a feature ranking function, e.g. Fisher’s score or Pearson Correlation coefficient^{19,20} , to choose the best features independent of the ML algorithm. Wrapper methods search the feature space to select the best feature subset, for final use, by testing the performance of each subset using an ML algorithm. Embedded methods select the best feature subsets on the fly as part of the final training process. Each method offers their own unique advantages and challenges. While the filter method is quick and model independent, it ignores relationships between features which are crucial for a complex target property like zT . Conversely, though wrapper methods consider feature dependencies, they become expensive with large datasets or large feature spaces. In embedded methods, lastly, though accounting for feature relationships and being relatively scalable, finding small feature subsets is challenging²¹ . A common strategy is to use the filter method as a pre-processing step for ranking features which can then be used with a wrapper method to finalize the cut-off via cross-validation (CV)^{22,23} . In this method, the minimum number of features to be retained is determined using an iterative redundancy analysis of the top ranked features using the saturation point of their CV score. A critical problem with model-specific-wrapper or embedded-methods stems from hyper-parameter tuning. The model performance of a given ML-algorithm is contingent upon the chosen hyper-parameters. Features selected for one set of hyper-parameters may not be the same as for another set. This, therefore, entails optimization of hyper-parameters at each iteration of the cross-validation process. While this adds another layer of complexity and cost to the already expensive wrapper method, such a brute force approach is both necessary and possible for small datasets, as in the case of TE materials, to improve the generalizability of the model.

In this work, we first propose a principal component analysis (PCA)-based train/test splitting method for hierarchical experimental TE datasets which considers multiple possible splits equivalent in chemical space. Thereafter, an integrated approach for optimization

of hyper-parameters along with a k -best feature filtering method for four different ML algorithms - Random Forest (RF)²⁴ , XGBoost (XGB)²⁵ , Neural Networks (NNs)²⁶ , and Sure Independent Screening-Sparsifying Operator (SISSO)²⁷ - is presented. Following the finalization of feature selection and hyper-parameter optimization, an ‘ensemble averaging’ approach for all machine learning techniques is adopted. Lastly, a high-throughput screening (HTS) strategy over a vast and chemically realistic compositional space is performed to predict top-performing never studied TE half-Heusler materials.

Methods

Composition-based feature vectors of half-Heusler materials

To numerically represent a $A_{1-x_A}A'_{x_A}B_{1-x_B}B'_{x_B}C_{1-x_C}C'_{x_C}$ half-Heusler material for machine learning, we construct a composition-based feature vector using 19 atomic properties for each of the six elemental components: A , A' , B , B' , C , and C' . The candidate elements for A , B , and C and their respective dopants A' , B' , and C' are taken from the list in²⁸ . The details of the crystallographic structure of the hH used in our work can be found in the same study.

These atomic properties, listed in Table S1 of the supplementary information (SI), were selected based on their reported importance in previous ML studies for different TE materials in the literature. They include fundamental physical and chemical quantities such as atomic number, atomic radius, atomic weight or valence electrons count. Values for these properties are extracted from the Mendeleev Python library²⁹ , normalized by the maximum absolute value to ensure comparability across features, while preserving their relative magnitudes. Each element is described by a 19-dimensional vector, and the full representation of a material combines six such vectors, resulting in a 114-dimensional vector that encodes a given composition. When a substituent site is empty, the feature values of the parent site were used for that site. To represent doping of a specific site, we append the three concentration

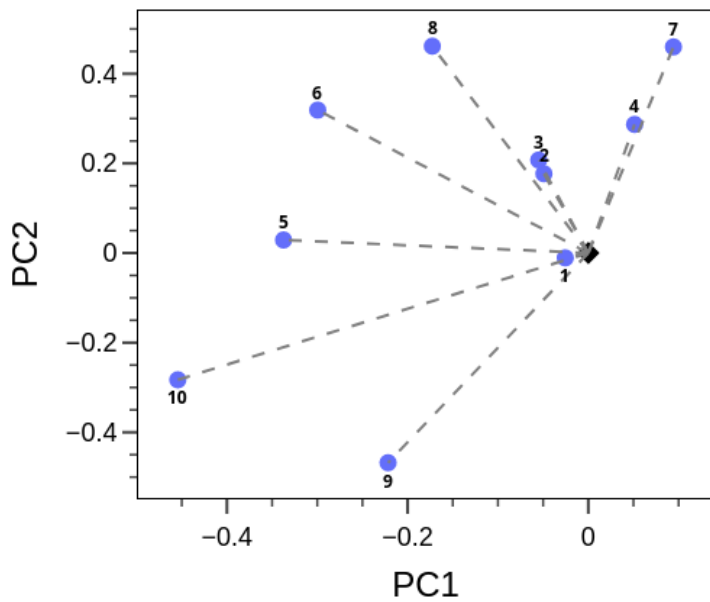
variables $x_{A'}$, $x_{B'}$ and $x_{C'}$, which correspond to the dopant concentrations on the A , B , and C sites, respectively. These three concentrations, ranging from 0 to 0.5, combined with the 114 atomic features, define a 117-dimensional vector that uniquely represents a composition.

In this work, we have used the ICGM dataset for half-Heusler TE materials that was curated in our previous work.⁹ A given chemical composition can appear at multiple temperatures in the dataset, reflecting the temperature dependence of the thermoelectric properties. As a result, the full dataset includes several data points per composition, each associated with a different temperature, which allows for learning temperature-dependent trends across a broad temperature range. Each of these 118-dimensional (117+ T) input vectors are then used as input for the machine learning model, and the zT values associated with each material and temperature are used as the target property. This curated dataset comprises 108 distinct materials, 256 unique compositions, and a total of 1521 data points, with temperatures from 289K to 1200K and zT from 0.0001 to 1.45. Our dataset is, to this day, the largest curated dataset, presenting no redundancies, available for half-Heuslers.

Separation of training and test datasets

To assess the generalizability of our models, that is, their ability to make accurate predictions on previously unseen compositions, we design a systematic and unbiased approach for splitting our dataset into training and test sets. These splits are based on the distribution of materials in the chemical space defined by the physical properties of the constituent elements of half-Heusler compounds (the 114-dimensional vector described earlier). We aim to construct five folds of our dataset: five separations between training and test sets for which the union of the test sets forms the full dataset and for which no material is present in two different test sets. This choice of feature subset leads to the presence of all compositions and temperature points of one material to be exclusively in either the training or the test set of a distribution. To construct a meaningful representation of this space, we apply principal component analysis (PCA), a dimensionality reduction technique that projects

high-dimensional data into a lower-dimensional space while preserving as much variance as possible. PCA identifies orthogonal directions of greatest variance in the data, known as principal components (PCs), which are ordered by their ability to explain the total variance. In our case, we retain the first 13 principal components, as determined by a cumulative variance analysis, shown in Figure S1 in the SI, which shows that these 13 PCs account for 95% of the variance in the dataset. This 13-dimensional PCA space becomes the basis of our data splitting. To construct the splits, we first compute the Euclidean distance of each material from the centroid of the dataset in this 13-dimensional PCA space (a 2D illustration is given in Figure 1 (a) where each point corresponds to the 2D projection of a material). Materials are then ranked by this distance, and their belonging to a test set is selected via a modular sampling scheme: for each of the 5 folds, materials whose rank modulo 5 equals to zero are assigned to the corresponding test set. Hence, in our five-fold setup, the first fold includes the 1st, 6th, and 11th most distant materials, the second fold includes the 2nd, 7th, and 12th, and so on (as illustrated in Figure 1 (b)). This method ensures that test sets are composed of representative and diverse samples in chemical space. We generate five such train/test folds, ensuring that each fold covers a similar and overlapping region of the chemical space. Although for clarity Figure 2 shows a 2D plot of the distribution of the materials in the five test sets, we use t-SNE³⁰ solely for visualization because it preserves local neighborhoods more faithfully in low dimensions than a linear projection³¹. This figure shows that materials do not group together for one test set, i.e. the test set of each fold is spread quite homogeneously over the whole space. The actual data split and modeling are performed in the full 13-dimensional PCA space computed from the selected features. In these figures each point represents a unique half-Heusler material and they can be explored in an interactive version provided via the GitLab link in the supplementary materials. The distribution of materials, composition, and data points in each fold is shown in Figure S2 in the SI.



Material	F1	F2	F3	F4	F5
1	Te	Tr	Tr	Tr	Tr
2	Tr	Te	Tr	Tr	Tr
3	Tr	Tr	Te	Tr	Tr
4	Tr	Tr	Tr	Te	Tr
5	Tr	Tr	Tr	Tr	Te
6	Te	Tr	Tr	Tr	Tr
7	Tr	Te	Tr	Tr	Tr
8	Tr	Tr	Te	Tr	Tr
9	Tr	Tr	Tr	Te	Tr
10	Te	Tr	Tr	Tr	Te

Figure 1: a) Illustration in 2D of the ordering of the materials by increasing distance from the centroid of the PCA space. b) Distribution of the materials in the training (Tr) or test (Te) sets for all the folds, based on the order defined in a).

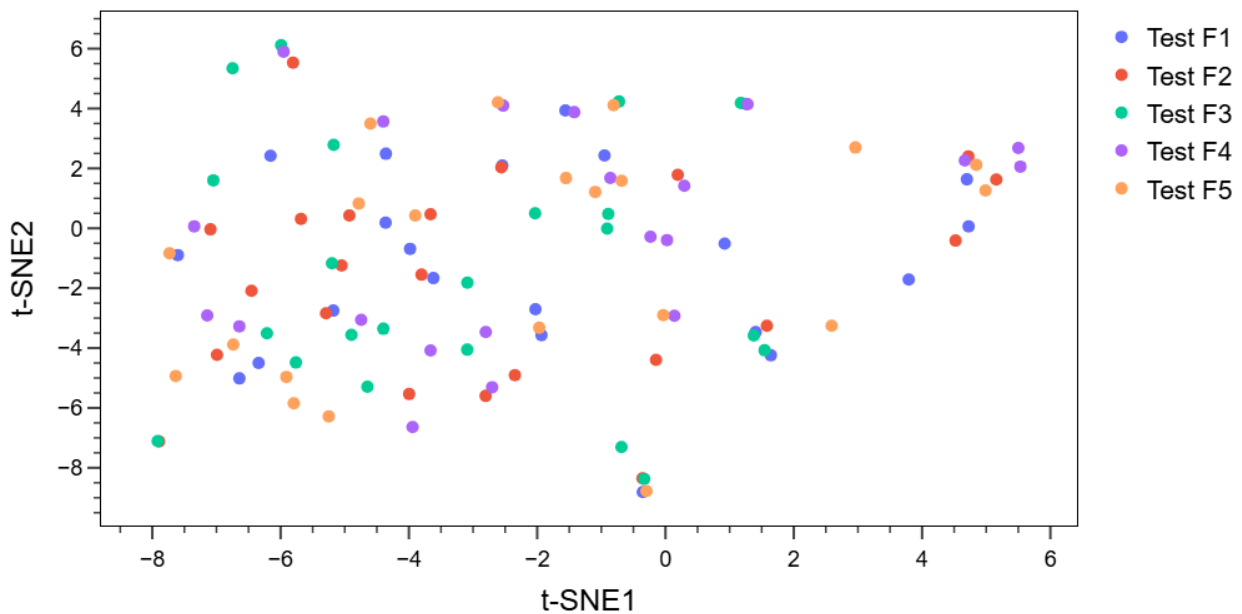


Figure 2: Two-dimensional t-SNE projection of each fold's test set

Feature selection

Correlation between elemental features and zT

For a complex material property like the TE figure-of-merit zT , one might be tempted to use the input of as many elemental features as possible for their possible relationship with the target property. However, too many input features require large computational resources and may lead to overfitting, especially when multicollinearity is present, as redundant or highly correlated features can cause the model to learn misleading patterns that do not generalize well to new data. In contrast, selecting too few input features may prevent the model from capturing essential patterns in the data, leading to underfitting and reduced performance on both training and test data.

The element-based definition of the 114 site-dependent features implies that the same set of descriptors characterizes all compositions and temperatures of a given material. This creates a hierarchical asymmetry in the dataset: while each material is associated with many zT values across different compositions and temperatures, its elemental nature is described by a unique set of elemental features (EF). To enable the calculation of statistical correlation coefficients between features and zT , we reduced this hierarchy by successive aggregation. First, we took the maximum zT for all measured temperatures for each composition. Then, for each material, we retained the maximum zT in all its compositions. This “double maximum” procedure ensures that each material, defined solely by its elemental configuration, is paired with a single representative zT value. The resulting one-to-one mapping provides a consistent basis for computing EF– zT correlations.

The Pearson correlation coefficient³² between a given elemental feature EF and the aggregated property zT is then computed as

$$r_{EF,zT} = \frac{\sum_{i=1}^n (EF_i - \bar{EF})(zT_i - \bar{zT})}{\sqrt{\sum_{i=1}^n (EF_i - \bar{EF})^2} \sqrt{\sum_{i=1}^n (zT_i - \bar{zT})^2}} \quad (1)$$

where \bar{EF} and \bar{zT} respectively denote the averages of the EF values and of the zT values

across the n materials. By definition, $r_{EF,zT}$ is bounded by -1 (perfect anti-correlation) and 1 (perfect correlation). In our analysis, we rely on the absolute value of the correlation coefficient, since both positive and negative correlations can carry predictive power: even an anti-correlated feature may provide useful information to the models for determining zT . We can then sort the features by importance score, as illustrated in Figure 3. The fold specific ranking of elemental features are shown in Figure S3 in the SI.

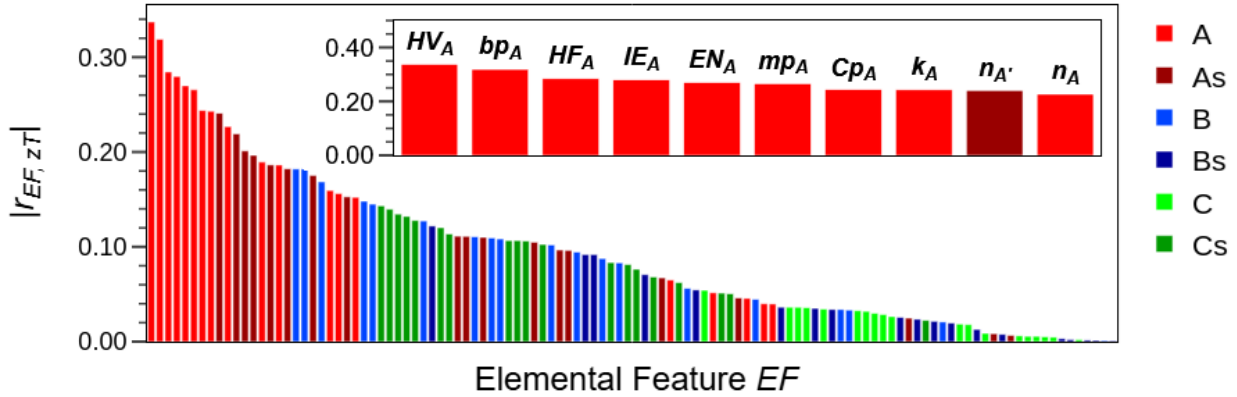


Figure 3: Ranking of the elemental features by absolute Pearson coefficient

Feature elimination

Following the ranking of the EFs, we proceeded to detect and remove redundant features by constructing Pearson correlation matrices between all feature pairs. It is important to note that the distributions of the feature values are site dependent. Properties such as the atomic radius (AR) or atomic weight (AW) exhibit low overall correlation ($r_{AR,AW} = 0.49$) for all the elements constituting hH materials regardless of the site. Nevertheless, due to the reduced list of elements authorized per site²⁸, the site-specific correlations between features can deviate substantially from this global trend. For example, the correlation coefficient of AR_C and AW_C for the elements possible on site C , differs significantly ($r_{AR_C,AW_C} = 0.89$) from the global trend.

To account for this, we constructed three separate correlation matrices, one for each site as shown in Figure 4 (a) for the A site (only five sample features are displayed, the

full correlation tables for all sites are available in Figures S4 in the SI). Because the set of candidate elements at a site remains unchanged regardless of whether substitution occurs, the distributions of possible elemental features at sites A and A' are identical. Consequently, the correlation matrices of their properties coincide. The same reasoning applies to the B/B' and C/C' sites. To discard highly correlated pairs, we started by constructing a graph by introducing a correlation threshold r_{\min} : vertices represent features and edges connect pairs with correlation above r_{\min} . The Bron–Kerbosch algorithm³³ was then applied to identify maximal cliques, i.e., fully connected subgraphs that are not contained within larger ones, each corresponding to a group of strongly correlated features. From each clique, only the feature showing the highest correlation with zT was retained. Repeating this procedure for the six sites yielded a reduced, non-redundant feature list for every chosen value of r_{\min} , as reported in Figure 4 (b). While the overall number of selected features increases with r_{\min} , occasional spikes appear because some thresholds produce different cliques that do not select the same representative feature, whereas higher r_{\min} -produced cliques yield only one feature.

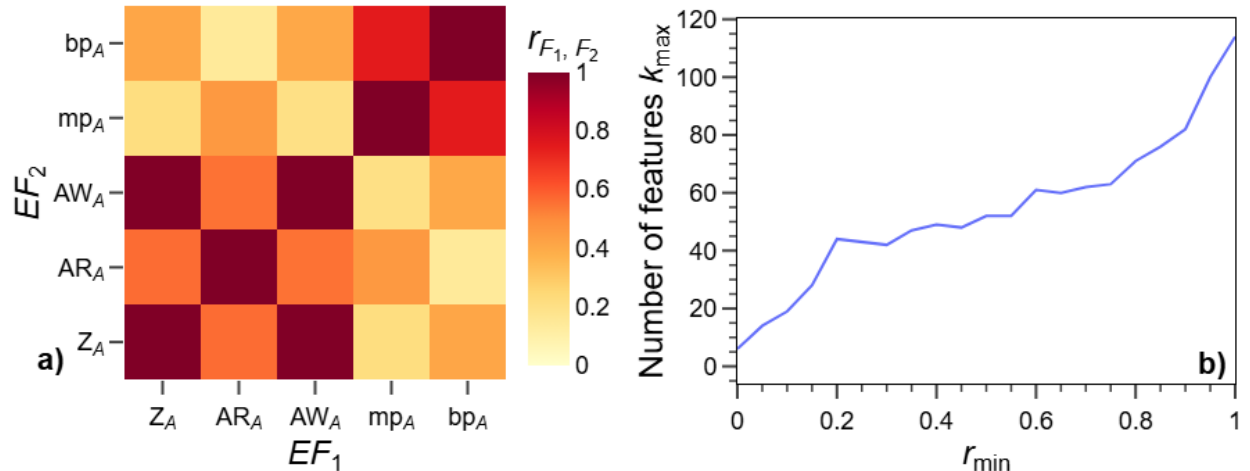


Figure 4: (a) Pearson correlation matrix of five sample elemental features of the A-site elements; (b) Evolution of the number of features k_{\max} retained as a function of the r_{\min} .

Crucially, the correlation threshold introduced earlier determines how redundancy is handled in the feature set and directly shapes the final model. A high threshold links only nearly identical features, limiting dimensionality reduction and leaving redundancies intact. A low

threshold, in contrast, treats even weak correlations as redundant, potentially discarding complementary information. In both cases, the ranking of EFs and the resulting feature subset are affected, which in turn impacts model performance. The correlation threshold must therefore be carefully tuned to strike the right balance between preserving informative diversity and eliminating ‘redundant’ features.

Evaluation metrics

In this study, we report global predictive performance of ML models comparing N experimental zT values (noted zT^{xp}) and predicted zT values (noted zT^{pr}) using Root Mean Squared Error (RMSE) and Maximum Absolute Error (MaxAE), while also considering Mean Absolute Percentage Error (MAPE) given by the following equations:

$$\text{RMSE} = \sqrt{\frac{1}{N} \sum_{i=1}^N (zT_i^{\text{pr}} - zT_i^{\text{xp}})^2} \quad (2)$$

$$\text{MAPE} = \frac{100}{N} \sum_{i=1}^N \left| \frac{zT_i^{\text{pr}} - zT_i^{\text{xp}}}{zT_i^{\text{xp}}} \right| \quad (3)$$

$$\text{MaxAE} = \max_{i=1}^N |zT_i^{\text{pr}} - zT_i^{\text{xp}}| \quad (4)$$

In addition, we define partial metrics to focus on regions of the zT spectrum with particular interest for HTS. For example MAPE is computed only on data points with $zT^{\text{pr}} > 0.2$ for doped compounds. This threshold reflects a practical cutoff for thermoelectric performance, highlights the model’s capacity to correctly predict materials that are experimentally known to be promising and avoids the situation where very small experimental values inflate artificially the MAPE.

The SISSO (Sure Independent Screening with Sparsifying Operator) method

The SISSO- Sure Independent Screening (SIS) in combination with Sparsifying Operator (SO) method was employed for descriptor identification from the dataset such that the target property (zT) can be expressed as a symbolic linear combination of complex descriptors:

$$zT^{\text{pr}} = \sum_{i=1}^n c_i d_i + A$$

where d_i is the i th descriptor, n the chosen number of descriptors (the so-called dimension of the regression) and A the intercept in the n -dimensional descriptor space.

The method, first, involves the construction of a large number of complex features ϕ^c (10^5 - 10^{12} elements) using a combination of algebraic/functional operations recursively on the feature set Φ (here the feature set Φ designates the 114 elemental features, the 3 concentrations, and the temperature). The operator set is defined as:

$\hat{H}^m \equiv \{I, +, -, \times, /, \exp, \log, ||, \sqrt{ }, ^{-1}, ^2, ^3, \text{scd}\}[\phi_1, \phi_2]$ - where $\text{scd}(\phi) = 1/(\pi(1 + \phi^2))$, ϕ_1 and ϕ_2 are features in Φ and the superscript m indicates that the dimensional analysis is performed to retain only meaningful ϕ^c s.

This generates candidate features of increasing complexity where the complexity is the maximum number of operations considered. We have chosen a complexity of five. Thereafter, it employs the so-called ‘Sure Independent Screening’ (SIS) - which is a screening process - to select a smaller number of ϕ^c s, the size of which depends on a user-defined SIS value (in our case 10000) multiplied by the dimension n (in our case $n = 2$). Finally, based on the descriptor dimension n , SISSO determines the best features from the vast ϕ^c feature space by using the sparsifying l_0 constraint²⁷.

SISSO calculations become computationally infeasible with 118 input features ϕ . Therefore, a variable selection method, as proposed by Guo *et al.* (2022)³⁴, performs iteratively a variable selection and subsequent SISSO calculations for model optimization. The method first obtains a subset S_a from the large pool of input features ϕ by random search prioritizing unvisited features (not yet included in S_a) over visited ones. The first SISSO calculation

(iteration no. 0) is performed, and the features appearing in the model are transferred from S_a to the initially empty, S_b . New random features are added to S_a and the subsequent SISSO calculations are performed with $S = S_a \cup S_b$. Features appearing in the improved SISSO model (better training RMSE) are transferred from S_a to S_b at each iteration. Finally, the iterations are deemed converged if the RMSE does not improve beyond a user-defined number of iterations, in our case 20.

High-throughput screening

After establishing the predictive performance of the models, they were used in a high-throughput screening (HTS) workflow to identify promising pure/doped half-Heusler compositions. The chemical space is defined by base compounds of the form ABC and their doped counterparts $A_{1-x_A}A'_{x_A}B_{1-x_B}B'_{x_B}C_{1-x_C}C'_{x_C}$. Candidate elements are drawn from the thermoelectrics literature (28) but with practical exclusions to preserve experimental feasibility and safety: Uranium (U), Thorium (Th) and Arsenic (As). The overarching objective was to construct a computationally tractable research space that maps cleanly onto what can realistically be synthesized and measured.

Concentration discretization

Dopant concentrations on each site were discretized in the interval $0 \leq x_{A'}, x_{B'}, x_{C'} \leq 0.5$. By default we used a uniform step of 0.05 (10 values), but this can be adapted to match the available experimental precision for synthesis. Another way to simplify the research space is to employ a non-uniform grid: for example, using a fine step of 0.01 between 0 and 0.1, where small dopant fractions can already induce significant variations in zT , and then switching to a larger step of 0.05 between 0.1 and 0.5. This hybrid strategy balances resolution at low doping with tractability at higher concentrations.

Database-informed stability filter for ABC matrix

Our dataset contains multiple doped variants that share the same A , B , and C sites, yielding a list of 29 unique ABC triplets. To avoid considering the whole cartesian product of ABC candidates containing many non-stable compounds, we define database-specific hull-distance cut-offs using two repositories: the Open Quantum Materials Database (OQMD)³⁵ and the Materials Project (MP)³⁶. For each unique ABC in our experimental dataset and for each database separately, we collect all reported formation energies from which the convex-hull distances are derived and we retain, for that triplet, the minimum hull distance. We then take the maximum of these 29 minima (one per ABC compound), yielding the stability cutoff for the given database. This procedure results in cut-off values of $0.15 \text{ eV.atom}^{-1}$ for OQMD and 0.9 eV.atom^{-1} for MP. In the HTS, a candidate ABC compound is retained if its reported hull distance is strictly below the corresponding cutoff in at least one of the two databases. The remaining ABC matrices are then associated by cartesian product to the dopant candidates (A' , B' , C') and to the concentration grids in order to generate the candidate list of $A_{1-x_{A'}} A'_{x_{A'}} B_{1-x_{B'}} B'_{x_{B'}} C_{1-x_{C'}} C'_{x_{C'}}.$

To account for thermodynamic stability and maximize synthesizability of the doped compositions, we only considered candidates with $17 < \text{valence electron count} < 19$.

HTS temperature interpolation

Because experimental zT is reported at multiple temperatures per composition while models operate at a given temperature, we interpolate each model's fold-specific test predictions to 673 K taken as the working temperature of hHs³⁷. Concretely, for each fold and each technique, we fit a quadratic surrogate f such as $zT^{\text{xp}} = f(T^{\text{xp}})$ on the fold's test compositions (each composition corresponding to a unique f) and evaluate models on the interpolated data points at 673 K, comparing zT^{pr} and $f(673 \text{ K})$. This reduces the number of effective data points used for error estimation (only the interpolated value at 673 K per test composition is needed) and aligns the evaluation of a model's predictive performance with the HTS

target temperature.

Within-technique ensemble averaging (5-fold) and across-technique averaging

Let e_F denote the RMSE of fold F at 673 K for a given technique, computed on the interpolated fold test set. For a fixed technique, the prediction for a candidate composition at 673 K is obtained by inverse-error weighting over the five fold models. For a ML technique t , we calculate the predicted value as:

$$zT_t^{\text{pr}} = \frac{\sum_{F=1}^5 \frac{zT_{t,F}^{\text{pr}}}{e_F}}{\sum_{F=1}^5 \frac{1}{e_F}} \quad (5)$$

with $zT_{t,F}^{\text{pr}}$ the prediction from fold F and e_F the error of the fold's model at 673 K. Each technique yields a fold-aggregated prediction zT_t^{pr} per candidate composition.

To combine techniques, we use a technique-level error e_t : the RMSE at 673 K recombined over 100% of the dataset by merging the test predictions as described before. The final technique-pondered prediction is derived from the same inverse-error scheme at the technique level:

$$zT_{\text{pon}}^{\text{pr}} = \frac{\sum_t \frac{zT_t^{\text{pr}}}{e_t}}{\sum_t \frac{1}{e_t}} \quad (6)$$

For each technique t we rank candidates by zT_t^{pr} at 673 K and retain a top- N list, enforcing one composition per material (A, A', B, B', C, C'). In parallel, we perform the same procedure across techniques using the technique-pondered predictions, yielding a second shortlist. Together, these two lists will serve as inputs in our future work for subsequent DFT calculations and experimental synthesis.

Results and discussion

In this work, each half-Heusler composition is represented by a set of elemental and concentration features that encode its chemical and physical makeup. The critical reduction of elemental features (EF) was performed in two successive stages. The first stage applies a correlation-based filtering procedure, a standard technique whose details are provided in the methods section. On top of this established approach, we introduced a second stage that combines feature selection with hyperparameter optimization. While both components exist separately in the literature, their joint application provides a more tailored descriptor set for the prediction of zT in half-Heusler compounds, thereby forming the basis for the subsequent machine-learning results.

***k*-best selection**

Having established the correlation-based filtering of features according to a correlation threshold r_{\min} , we then turn to a systematic procedure to identify the most effective number of features through a k -best evaluation strategy. This procedure identifies the optimal number of EFs that minimizes cross-validation (CV) error. The method proceeds through several complementary steps. First, the correlation threshold r_{\min} is varied across a defined interval (e.g., twenty evenly spaced values between -1 and 1). For each r_{\min} value, we order a unique list of non-redundant features obtained by using the matrix method described previously. As illustrated in Figure 4(b), the size of these lists increases with the threshold value, yielding for each threshold an ordered sequence of candidate features.

Evaluation of feature subsets is then performed by progressively increasing the subset size: models are trained using only the first k features in the list, where $k \in \{1, 2, \dots, N\}$ and N is the total number of features retained at the chosen r_{\min} . Crucially, the ordering of features is determined by their correlation strength with zT so that the k -best subset always corresponds to the k most zT -relevant EFs present in the threshold-filtered list. Each combination of r_{\min} and k corresponds to a unique list of elemental features. For each

k -long list of features, we perform hyperparameter optimization of RF, XGB, and NN (the multiple layer perceptrons NN architecture used in this study is shown in Figure S5 in the SI) using Bayesian optimization^{38,39} restricted to 80% of the data (research grids are available in Tables S2 to S4 in the SI). This procedure is repeated five times according to the PCA-based fold construction method described above, with five mutually exclusive 20% test sets strictly held for the final evaluation. To ensure unbiased model selection, each 80% training set is internally partitioned using a 10-fold cross-validation scheme constructed with the same PCA process. Each fold involves training on 90 % of the training set (72% of the total data) and validation on the remaining 10% (8% of the total data).

The RMSE is calculated on the full training set (after recombining the ten validation subsets, each representing 8% of the total data). The evolution of this RMSE is presented in Figure 5(a). To mitigate the non-deterministic nature of the ML algorithms, this entire optimization is repeated three times, and the average RMSE across repetitions is used to determine, for each fold, the pair (r_{\min}, k) yielding the best performance. The selected hyperparameters are then fixed, and the final model is retrained on the complete 80% training set, ultimately producing five models per ML technique, one for each fold. Figure 5(b) illustrates the results on a demonstration fold with the XGBoost technique. As each curve corresponds to a unique value of r_{\min} , we can identify a pair (r_{\min}, k) at which the RMSE reaches its lowest values. For a given threshold, the k_{best} selected by the procedure is generally smaller than k_{tot} , the total number of features retained at that r_{\min} . Beyond the decrease of the validation RMSE, this reduction in dimensionality, as shown in Figure 5(c), is valuable in itself as it lowers the number of features entering the model while preserving predictive performance, thereby reducing the computational cost of the subsequent high-throughput screening.

This procedure guarantees a rigorous and unbiased feature selection while preserving the integrity of the independent test set. By rotating through all folds to train models, every data point can be predicted by a model for which it belonged to the test set, emulating

the conditions of high-throughput screening (HTS), where the model must generalize to entirely new materials. After collecting these zT predictions across the entire dataset, we compare them to the true values to compute a single final RMSE, measuring the predictive performance in HTS conditions.

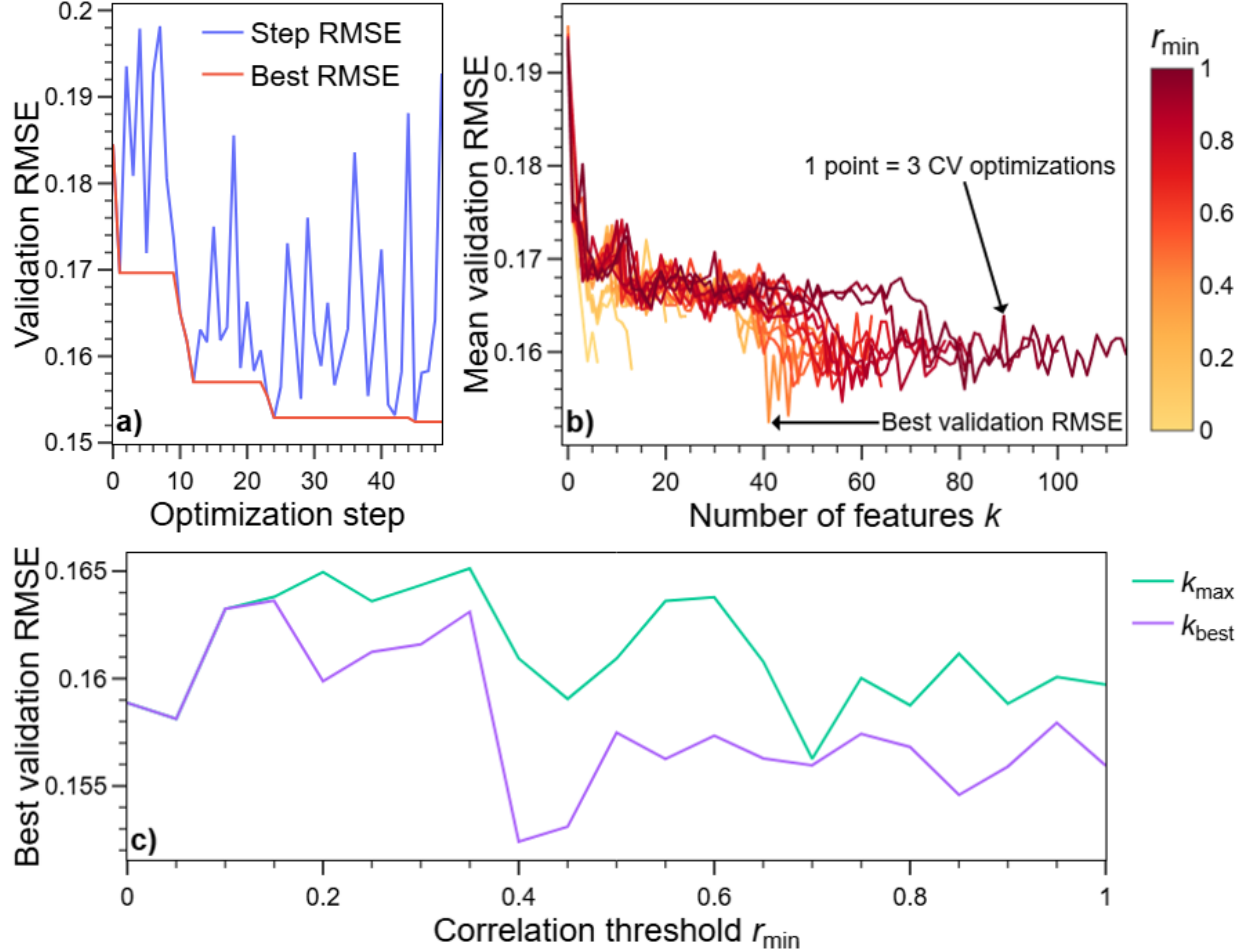


Figure 5: a) Optimization of the XGBoost hyper-parameters with the features set by the pair $(r_{\min}, k) = (0.4, 41)$; b) k -best selection: the pair $(r_{\min}, k) = (0.4, 41)$ leads to a validation RMSE of 0.152; c) Effect of k_{best} over the use of k_{\max} : decrease of the validation RMSE and of the threshold r_{\min} leading to a decreased number of features.

Feature filtering using iterative variable selection (VS) algorithm for SISSO

The k-best wrapper approach discussed above is not computationally feasible with the SISSO method, since SISSO relies on the brute search of the high-dimensional feature space. For this

method, we used a new algorithm proposed by³⁴ (2022) that integrates SISSO with iterative variable selection (random search) for optimization of the model with a large number of input features. The details of this method were given in the Methods section. Figure 6 shows the plot of lowest training RMSEs obtained as a function of iterations for a random search of features. The steep drop in RMSE for all the folds after a few iterations is due to the inclusion of temperature (T) in the feature subset used for training the SISSO models. All the models converge within 60 iterations and the final training RMSEs obtained were in the range of $\tilde{0.13}$ to $\tilde{0.16}$. Table 1 shows the number of occurrences of features in the final SISSO descriptors for all the folds. Temperature, obviously, was the most recurrent feature appearing in all the five folds followed by $x_{A'}$, HF_A , HV_C appearing in three of the folds. The EFs ea_A , $ea_{A'}$, $ea_{C'}$, HV_A and HF_C appeared in at least two of the folds whereas the rest of the features were only present in a specific fold. While the zT dependence on substituent concentration is obvious, $x_{B'}$ and $x_{C'}$ were surprisingly missing from all the folds. Therefore, the presence of other features for B and C sites suggest that the identity of the substituent at these sites is, statistically, more influential than its concentration - at least for our dataset.

Evaluation of resulting models

All ML models are evaluated on a reconstructed test set which is obtained by combining the predictions from each of the five folds. This allows us to evaluate every data point as unseen data, since its prediction comes from a model that was not trained on it. The final evaluation is then applied consistently across different machine learning methods: NN, XGB, RF, and SISSO. The fold specific RMSE values for all the models, listed in Table S5 in the SI, prove that the value of the test RMSE is dependent on the selected fold. Hence, RMSE values can be large or small depending on the choice of the fold. Moreover, it's pertinent to highlight the fact that we have split our data points at the material level and not the composition level which is often the case in the literature, as mentioned in the Introduction section. This makes our test sets more challenging to extrapolate beyond dopant concentrations. Our

Table 1: Number of occurrences of elemental features in the final SISSO descriptors across all the folds

	Elemental Features (EFs)	Number of occurrences	Fold
1.	T	5	F1, F2, F3, F4, F5
2.	$x_{A'}$	3	F2, F3, F5
3.	HV_A	3	F1, F4, F5
4.	HF_C	3	F1, F3, F5
5.	ea_A	2	F1, F3
6.	HF_A	2	F2, F5
7.	$ea_{A'}$	2	F2, F3
8.	HV_C	2	F2, F5
9.	$ea_{C'}$	2	F1, F2
10.	mp_A	1	F5
11.	$mp_{A'}$	1	F1
12.	$k_A?$	1	F5
14.	bp_B	1	F3
15.	n_B	1	F4
16.	IE_B	1	F2
17.	$IE_{B'}$	1	F5
18.	$n_{B'}$	1	F3
19.	AR_C	1	F2
20.	mp_C	1	F2
21.	Z_C	1	F4
22.	$Z_{C'}$	1	F4
23.	Z_A	1	F4
24.	$Z_{A'}$	1	F4
25.	$AR_{A'}$	1	F1

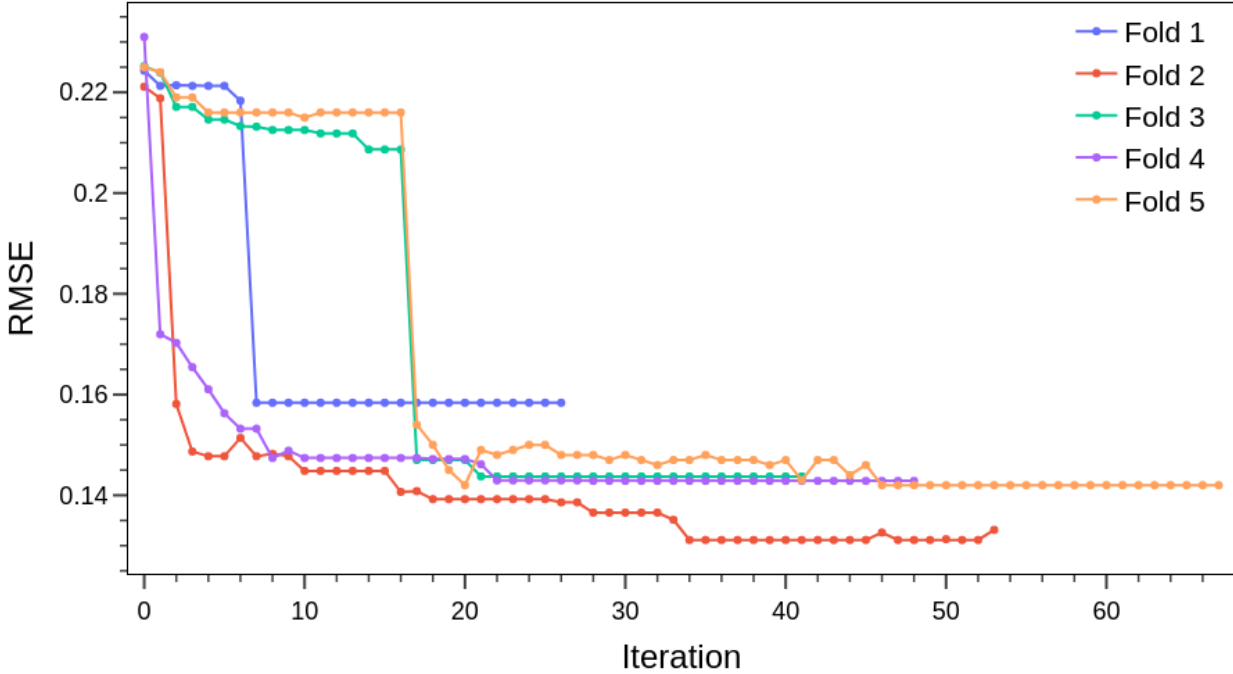


Figure 6: Evolution of the RMSE of the SISSO model during the iterative variable selection process

approach, therefore guarantees a fair estimate of the predictive performance of the models. The final evaluation is then applied consistently across different machine learning methods, including SISSO, XGBoost, RF, and NNs. The parity plots for all the techniques are shown in Figure 7 and the predictive performance metrics are summarized in Table 2. Overall, SISSO and NN achieve almost similar performance with respective test RMSEs of 0.163 and 0.164 respectively. These RMSEs are slightly higher than the best RMSE value of 0.14 obtained by⁴⁰ and are comparable to the 0.156 achieved by¹⁴. However, Zhong et al. (2023) have used in-lab generated experimental data with uniform synthesis conditions and measurements whilst ours is from across the literature notwithstanding the inter-laboratory uncertainty errors (round-robin errors)⁴¹. Additionally, in both of these works, not only is there an ambiguity on the splitting hierarchy of test-train data but the RMSE was also calculated on specific test sets unlike ours where a cumulative RMSE is used for the whole dataset which is a better indication of precision and generalizability of our models.

After SISSO and NN, XGBoost showed the best performance with an overall test RMSE of 0.166, whereas the RF models were the worst overall with an RMSE of 0.169. SISSO’s and XGBoost’s good performance can be attributed to their in-built l_0 and l_1 regularization which is extremely crucial for small datasets. As for NN, the good performance could potentially be a consequence of its ability to capture intricate and non-linear relationships from the data, as discussed subsequently in the section on SHAP analysis for NN, XGBoost, and RF Models, which is specifically crucial for understanding and predicting a complex physical quantity like zT ⁴². This performance can further be improved by incorporating regularization such as l_1 , l_2 , elastic net, and dropout methods, or their combinations⁴³. Given that NNs are ‘data-glutton’⁴⁴, combining ensemble learning strategies with NNs (called as NN ensembles) may prove to be even more promising due to their ability to handle small structured (preprocessed) data more efficiently.⁴⁵

A systematic trend present in all models is the overprediction for $zT^{\text{xp}} < 0.2$ and under-prediction for $zT^{\text{xp}} > 0.2$, often producing a cluster of similar zT^{pr} values even when zT^{xp} covers a wider range. The phenomenon was more pronounced for non-SISSO models showing a large number of outliers. Such datapoints were also visible in the parity plots of^{10,13,14} but were presumably treated as dataset outliers and not discussed further. Since our data is thoroughly curated, this cannot be attributed to experimental/measurement/data extraction errors but is solely function of a models’ sensitivity to the data. Further investigation into the raw data revealed that this behavior was mostly limited to compounds with very small experimental zT values in their pristine form, and showing a multifold increase in zT^{xp} upon doping. For example, Zhu et al. (2019) reported a dramatic increase in zT^{xp} of TaFeSb, from 0.0176 at 970 K, to 1.39 for A-site doped $Ta_{0.84}Ti_{0.16}FeSb$ at the same temperature⁴⁶. A similar situation exists for other materials such as TiCoSb⁴⁷, NbFeSb⁴⁸, ZrCoBi,⁴⁹, etc. On the other hand, there were several compounds, such as TiNiSn⁵⁰ and ZrNiSn⁵¹ with reasonable zT^{xp} values in pristine form and only showing a small increase with doping. While physically there is no restriction on the magnitude of doping-induced

zT improvements, this represents a significant challenge for ML models to incorporate a balance between these two types of materials especially without synthesis information. This results in zT^{pr} overpredictions for such pure compounds whereas their doped counterparts give higher but underpredicted zT^{xp} values. When excluding the pure compounds, the MAPE improves noticeably as shown in the partial MAPE analysis in Figure S6 in the SI. This is justified in the context of high-throughput screening, where the focus lies on doped compounds. Regardless, though our models tend to remain conservative, they achieve stable global accuracy with the obtained test RMSEs remaining in between 11% and 12% of the highest zT^{xp} value (1.45).

Table 2: Predictive performance metrics for the recombined test dataset across different ML techniques.

Metric	Filter	NN	XGB	RF	SISSO
RMSE		0.164	0.166	0.169	0.163
MAPE	$zT^{\text{pr}} > 0.2$ (doped)	26.6%	28.6%	30.7%	30.9%
MaxAE		0.892	0.805	0.816	0.672

SISSO Descriptors Interpretation

Table 3 depicts the final SISSO descriptors of the form $zT = c_1 d_1 + c_2 d_2 + A$ across all the folds -where d_1 and d_2 are one- and two- dimensional descriptors, c_1 and c_2 their respective coefficients, and A the intercept. This represents a symbolic linear expression of zT with respect to individual descriptors but zT is highly non-linear with respect to the elemental features. Apart from F3, the zT vs T relationship in all the folds is linear. From a physical perspective this is not true, since zT values pass through a maximum before declining due to several physical phenomena - such as bipolar conduction, increased electronic thermal conductivity, etc. However, the experimental temperature data of zT is usually limited to peak zT values in the literature and by extension in our dataset. Hence, the model is unable to learn the declining parabolic trend beyond zT_{max} temperatures. A surprising observation is the absence of B or B' - site EFs in F1. Physically, the importance of the B -site in

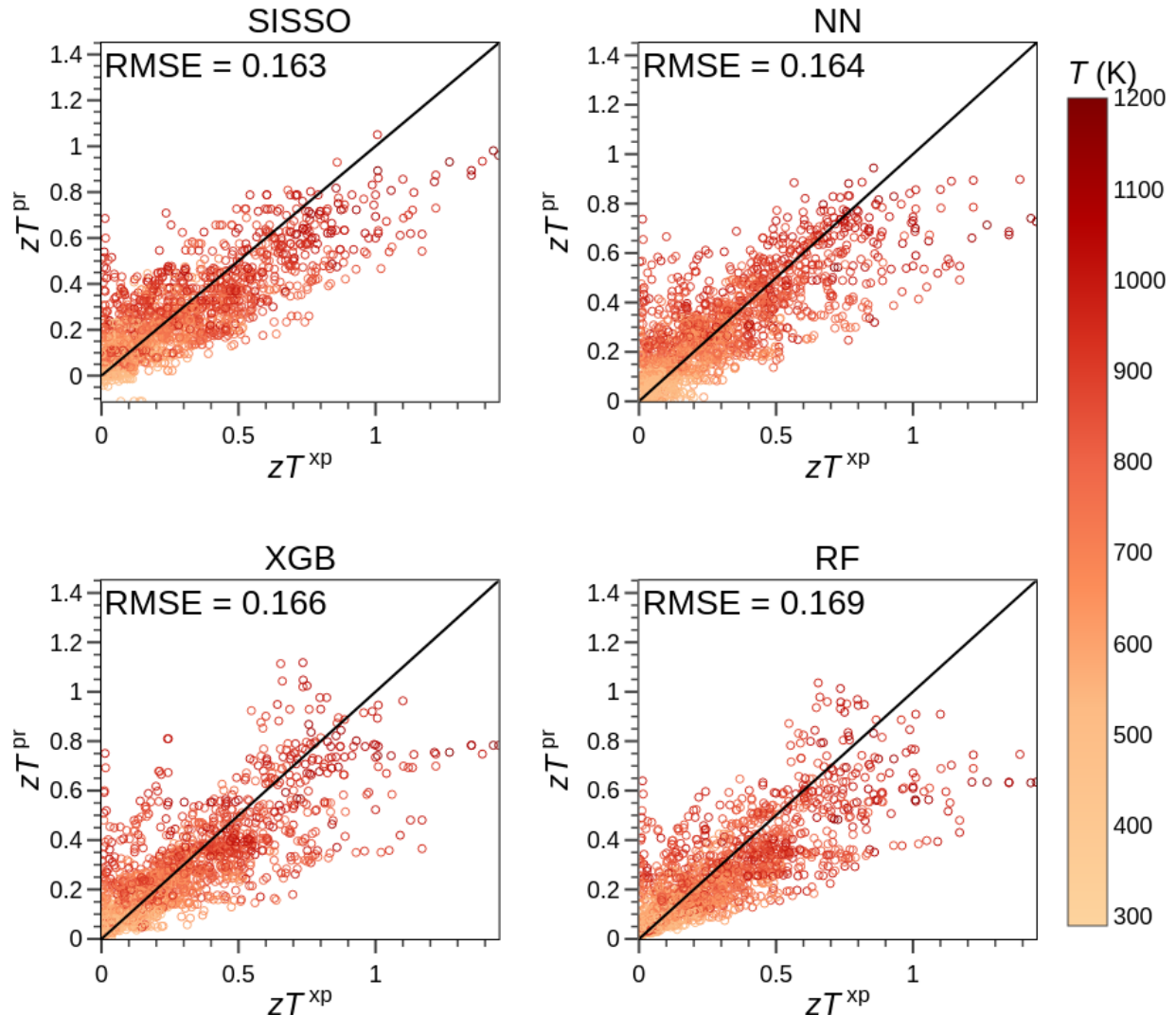


Figure 7: Parity plots of predicted zT (zT^{pr}) vs experimental zT (zT^{xp}) for each ML technique.

hH cannot be underestimated. However, statistically, at least for F1, this means that the influence of A - and C - sites overwhelms the contribution of B - site EFs to the zT . This can clearly be observed from the ranking of the elemental features by the Pearson coefficient, shown in Figure S3 in the SI where A -site EFs show a dominant correlation to zT followed by C -site EFs (for F1). A significant advantage of ensemble averaging is the inclusion of all local trends in the ultimate average model. Therefore, by virtue of descriptors from other folds representing B or B' sites, their influence is not completely ignored in the final HTS predictions.

For the physical interpretation of descriptors, it is important to avoid an apophenic approach since several terms appearing may just be a consequence of the statistical artifact of the specific fold, or the dataset (as we saw with $x_{B'}$ and $x_{C'}$), and may not necessarily reflect a global trend across hH materials, or other TE materials for that matter. SISSO involves a dimensional analysis to retain only meaningful correlations between target property and combinations of EFs (e.g., no unphysical items such as size + energy or size + $size^2$). Therefore, the resulting descriptors are supposed to be "physically meaningful"²⁷. However, there are several EFs which are identical in dimensions (units) but mostly unrelated to each other - such as HF_C and e_A appearing as $|HF_C - ea_A|$ in F3 (d_2). Additionally, the complexity of the descriptors also limits an exhaustive interpretation. Therefore, we must restrict our analysis to only physically intuitive and/or most consistent terms in the descriptors.

The presence of $scd\left(\frac{x_{A'}}{ea_{A'}}\right)$, $\sqrt[3]{\frac{x_{A'}}{ea_{A'}}}$, and $\exp\left(\frac{x_{A'}}{ea_{A'}}\right)$ (with negative coefficients) in F2 (d_2), F3(d_1), and F5 (d_2), respectively, is interesting, especially due the coupling of $x_{A'}$ to $ea_{A'}$ and $k_{A'}$. The terms scd and $\sqrt[3]{\cdot}$ represent conflicting behavior at high values of $x_{A'}/ea_{A'}$. For the $x_{A'}$, a common behavior is its strong non-linear effect on the zT suggesting that the increase in zT will be more prominent for the initial increase in substituent concentrations. This effect can be explained by the fact that a small dopant concentration can result in the formation of impurity bands within the band gap^{40,52}. For $ea_{A'}$, the scd and $\sqrt[3]{\cdot}$ functions require higher and lower values of $ea_{A'}$, respectively,

making interpretation difficult. However, we see a more consisting trend of the positive effect of electron affinity on zT , as evidenced by the term ea_A in F1 and F3. Physically, an atom with a smaller electron affinity can completely lose its valence electrons and serve as a Coulomb active scattering center for charge carriers and, thus, reduce charge mobility. Conversely, an atom with higher electron affinity should (A-site in this case) still attract part of its negative charge and reduce Coulomb scattering for charge carriers. This can improve carrier mobility, and therefore electrical conductivity, leading to a higher zT ⁵³. While it is tempting to attribute a small $k_{A'}$ to a smaller bulk thermal conductivity and hence to a higher zT , the bulk thermal conductivity of a material is not simply a direct sum of the thermal conductivities of its constituent elements. It's rather a complex function of the material's composition, microstructure, and porosity^{54,55}.

The term $|Z_A - Z_{A'}|$ in F4 (d_1) indicates that zT can be maximized with heavier atoms at A -site and lighter atoms at the A' -site or vice versa. The disparity of weights between A and A' atoms can maximize the point defect scattering, which can result in a decrease of the thermal conductivity and hence an increase of zT ⁵⁶. The role of alloying, particularly on the A-site, in suppressing the thermal conductivity of hH materials has been consistently reported in the literature⁵⁷. It is also important to recall that HV_A and HF_C have the highest occurrence number in all the descriptors, and, therefore, their influence cannot be ignored. We consistently observe a requirement of large HV_A in F1 (d_1), F4 (d_1), and F5 (d_1) descriptors. This can be attributed to the ability of elements at the A -site to form stronger bonds with neighboring atoms and, thereby, reduce disorder and maintain higher electrical conductivity at high temperatures^{40,58,59}. On the other hand, we observe a requirement of low HF_C/HV_A , in F1 (d_2), and $|HF_A - HV_C|$, in F2 (d_1) and F5 (d_1), respectively. When coupled together, these observations demand higher HF_A and HV_A along with a lower HF_C and HV_C . In TE materials, while strong bonds can sustain good electrical conductivity and stability at elevated temperatures, weaker bonds can reduce lattice thermal conductivity, and increase zT ⁶⁰. This, therefore, requires a fragile balance of bond strengths, and our

descriptors implicitly quantify the effect of this balance on zT . To sum up, while we could identify and interpret physically intuitive and consistent trends in the SISSO models, the complexity of SISSO descriptors and uncertainty associated with statistical artifact of the dataset restricted an exhaustive interpretation. Yet, this limited physical interpretability of SISSO is better than other ‘black-box’ algorithms where model analysis is only restricted to feature importance.

Table 3: Final SISSO descriptors of the form $zT^{\text{pr}} = c_1d_1 + c_2d_2 + A$ across all the folds

Fold	Parameters	RMSE (Train/test)	Descriptors
F1	$c_1 = 0.962$ $c_2 = -0.001$ $A = 0.141$	0.158/0.158	$d_1 = T \times AR_{A'} \times HV_A \times \exp\left(\frac{HF_C}{mp_{A'}}\right)$ $d_2 = \frac{T}{ea_A \times \left(\frac{HF_C}{HV_A} - \text{scd}(ea_{C'})\right)}$
F2	$c_1 = 5.04$ $c_2 = 1.13$ $A = 0.026$	0.131/0.170	$d_1 = T \times AR_C \times ea_{C'} \times \sqrt[3]{ HF_A - HF_C }$ $d_2 = \frac{mp_C \times \text{scd}\left(\frac{x_{A'}}{ea_{A'}}\right)}{HF_A - IE_B}$
F3	$c_1 = 0.104$ $c_2 = 0.314$ $A = 0.011$	0.144/0.156	$d_1 = \left(\frac{T}{n_{B'}}\right)^3 \times \sqrt[3]{\frac{x_{A'}}{ea_{A'}}}$ $d_2 = \frac{1}{\exp\left(\frac{bp_B}{T}\right) \times \sqrt[3]{ HF_C - ea_A }}$
F4	$c_1 = 0.398$ $c_2 = -4.43$ $A = -0.132$	0.143/0.176	$d_1 = \frac{T \times HV_A \times (Z_{C'} + Z_A - Z_{A'})}{bp_C}$ $d_2 = \frac{T \times Z_C - n_B }{Z_C / \log(Z_{C'})}$
F5	$c_1 = 1.96$ $c_2 = -0.942$ $A = 0.05$	0.142/0.153	$d_1 = \frac{T \times HV_A \times \sqrt{ HF_A - HV_C }}{mp_A}$ $d_2 = \frac{ HF_C - (IE_{B'} - HV_A) }{\exp\left(\frac{x_{A'}}{k_{A'}}\right)}$

SHAP analysis for NN, XGBoost, and RF Models

The SHAP (SHapley Additive exPlanations)⁶¹ violin plots for the model-dependent feature importance is shown in figure 8 for the RF, XGB, and NN models. In these plots, the features are ranked from top to bottom (Y-axis) based on their global importance. The top

feature is the strongest "driver" of the model's zT predictions. The SHAP values (X-axis) show how much a feature pushes the prediction away from the average (origin) with positive and negative values corresponding to positive and negative correlation to zT , respectively. The wide section of the violin shape indicates a large number of data points with similar SHAP values. The color reflects the magnitude of the features (red for high, blue for low). In combination with SHAP values, directional trends can be deduced: blue points on the left/red points on the right, indicate a positive correlation between an increase/decrease of the feature with an increase/decrease of zT . Similary to the interpretation of the SISMO descriptors in the previous section, we will limit our analysis to the most consistent or important trends.

Temperature (T), being both a physical constant in the zT formula and a dynamic environmental variable that changes the material's TE properties, is the most important feature in all three models. For RF and XGB, the distinct segregation of low-value (blue) points on the negative SHAP side and high value (red) points on the positive side suggests a monotonic positive correlation with zT . Interestingly, for NN, the red and blue points are mixed on both sides, which indicates that the feature has a complex, non-monotonic relationship with zT — governed by interactions with other features rather than acting as an independent driver.

$x_{A'}$ (A-site dopant concentration) is the next omnipresent feature across all the models. For $x_{A'}$, however, the SHAP distribution reveals a more nuanced behavior for all models. The presence of blue points on both sides of the zero-baseline suggests that the influence of $x_{A'}$ on zT is context-dependent, governed by feature interactions -similar to what we observe for T in NN models. Nevertheless, the greater density (indicated by the vertical width of the violin) on the negative side of the x-axis demonstrates that, when averaged across the entire dataset, low $x_{A'}$ values more frequently suppress zT . This confirms that while a low A-site dopant concentration is statistically detrimental to high zT , it is a probabilistic trend that can be modulated by the specific material environment. Indeed, the presence of blue points

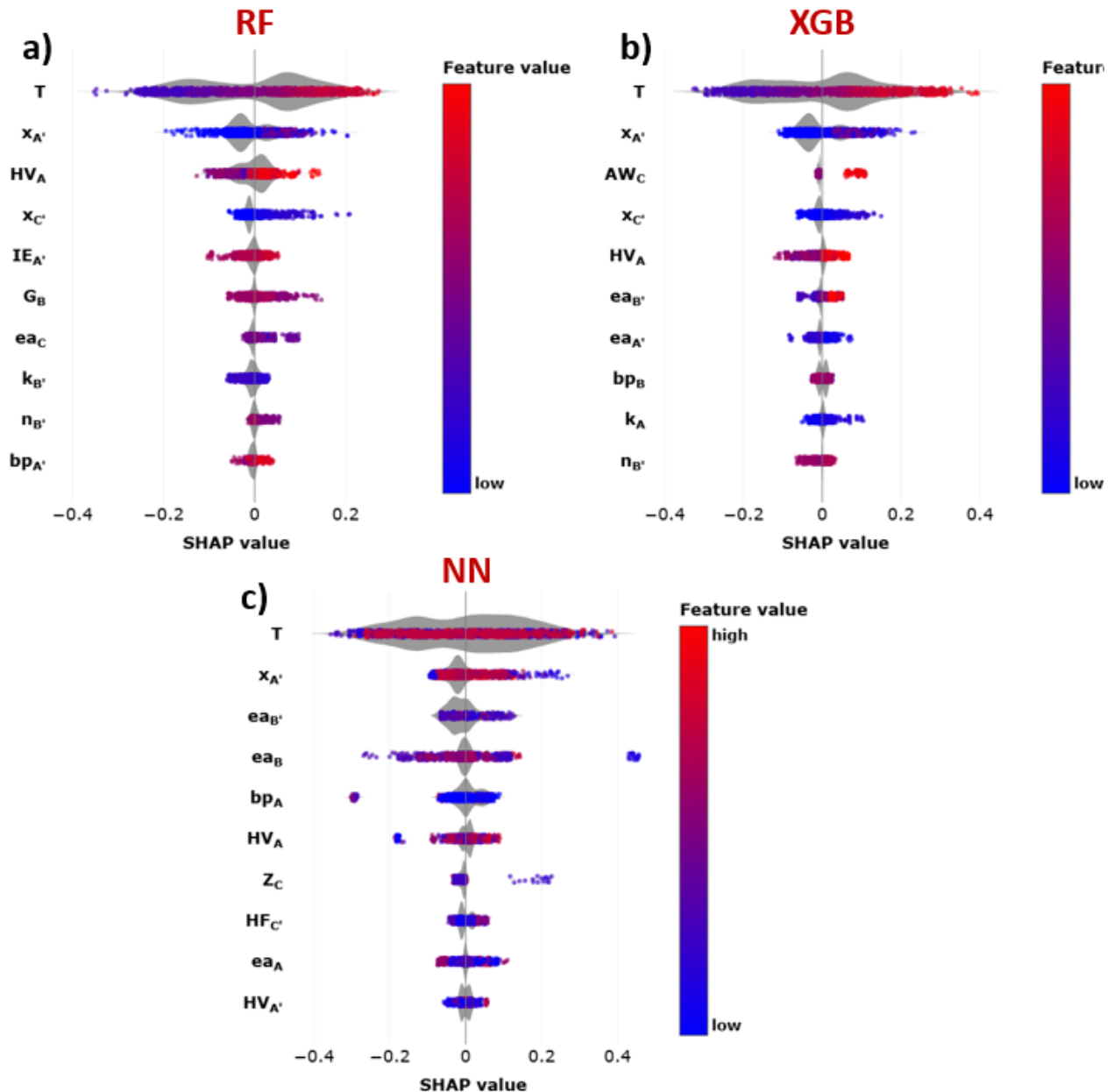


Figure 8: Comparative SHAP global analysis for the test sets for a) RF, b) XGB, and c) NN.

on the extreme right for all the plots proves that for some materials exceptionally high zT with small dopant concentration (at the A-site) can be achieved - a fact corroborated by SISSO descriptors as well as experimentally established for TaFeSb⁴⁶, TiCoSb⁴⁷, NbFeSb⁴⁸, and ZrCoBi⁴⁹ as discussed before.

From the model-agnostic ranking of the top 10 EFs in Figure 3, only HV_A (heat of vaporization for A-site) appears in all three SHAP plots—consistent with the trend in SISSO descriptors. Similar to our observation with $x_{A'}$, we see a very subtle SHAP distribution with presence of red points on both the sides of the baseline for RF and XGB. Yet again, statistically, considering the greater density of data points on the positive side for these plots, HV_A ’s correlation to zT is largely positive for RF and XGB. NN shows a more subtle, mixed trend with presence of blue and red points on either side. This result, on the one hand, unanimously establishes the importance of HV_A in both model-agnostic and model-dependent frameworks. On the other hand, the fact that no EFs (other than HV_A) are simultaneously present in all the plots emphasizes the importance of inter-correlation between EFs rather than their individual importance for zT prediction. This demonstrates that each technique handles these variables differently, with the NN capturing more complex, non-linear relationships.

High-throughput screening (HTS)

The compositional space was explored by varying the substitution concentrations in two regimes: a fine grid with a step of 0.01 from 0 to 0.1, and a coarser grid with a step of 0.05 from 0.1 to 0.5. Out of approximately 6.6×10^8 possible compositions, the top-ranked compositions for four best performing hH matrices are given in table 4 for within-technique and across-technique ensemble averaging .The underlying idea behind using ensemble averaging is that a collection of diverse ML models trained on different data subsets can produce more accurate and stable predictions than a single model. It is very useful in lowering the variance of a model implying its predictions are less sensitive to the specific training dataset leading to

more reliable and consistent results⁶² . Precisely, in our case, a significant advantage of ensemble-averaging will be the inclusion of all local trends in the ultimate average model. Moreover, interpolating at a single, application-relevant temperature (673 K) yields an error metric tailored to the screening objective. The two-stage inverse-error weighting privileges folds and techniques that demonstrably perform better at the target temperature, while maintaining diversity across models. The resulting shortlists therefore provide a statistically well-grounded prioritization of candidates.

Database-informed filtering balances the breadth of exploration with practical stability constraints, but we deliberately excluded *ABC* compounds for which hull distance information is not available in OQMD or the Materials Project. These excluded matrices could result in compositions with high zTs , but at present we avoid them because of the additional computational cost of evaluating their stability. Similarly, the present filtering step rejects *ABC* matrices with hull distances above the database-specific cut-offs, but such systems might still be synthesized today or in the future. Including them would enlarge the search space at the expense of reduced certainty in stability. Most of the predicted best performing hH matrices, e.g., NbFeSb,⁴⁸ TaFeSb⁴⁶ and ZrCoBi,⁴⁹ have been reported as excellent TE materials with different dopants and compositions. Therefore, our results also hold promise with these new compositions. We also find new compositions with new matrices, HfNiSb, TiNiGe, and ZrNiBi, which have never been experimentally investigated thus offering a new avenue of exploration. Elements with a small atomic radius Li or Mg, feature predominantly for SISSO and NN predictions. This can probably serve as a recipe for enhanced point defect scattering at the A-site, as discussed in the SISSO Descriptor Interpretation section. However, the risks of interstitial defect and secondary phase formation cannot be ruled out, especially since these p-type dopants have never been experimentally reported for any hH composition in the literature.

For experimental validation, we plan to use thin-film material libraries (TFML)⁶³ for high-throughput synthesis, employing co-sputtering of constituent elements, and characteri-

Table 4: Best HTS predictions for within/across-technique weighted averaging

t	A	A'	B	B'	C	C'	$x_{A'}$	$x_{B'}$	$x_{C'}$	zT_t^{pr}
SISSO	Hf	Li	Ni	Zn	Sb	Bi	0.45	?	?	1.24
	Ta	Li	Co	Fe	Sb	Sn	0.5	?	?	1.19
	Nb	Li	Co	Pt	Sb	Sn	0.5	?	?	1.18
	Ti	Mg	Ni	Zn	Ge	Si	0.5	?	?	1.08
NN	Ta	Li	Fe	Ag	Sb	Sb	0.25	0.05	0	0.77
	Nb	Li	Fe	Cu	Sb	Sb	0.2	0.05	0	0.75
	Zr	Li	Co	Cd	Bi	Bi	0.25	0.25	0	0.74
	Ta	Mg	Co	Cu	Sb	Ge	0.25	0.05	0.05	0.74
XGB	Ta	Ti	Fe	Fe	Sb	Al	0.15	0	0.05	0.68
	Nb	Ca	Fe	Fe	Sb	Sb	0.15	0	0	0.64
	Zr	Zr	Co	Pt	Bi	Sn	0	0.05	0.45	0.64
	Zr	Hf	Ni	Ni	Bi	Sn	0.05	0	0.45	0.63
RF	Ta	Ti	Fe	Fe	Sb	Bi	0.15	0	0.05	0.74
	Zr	Zr	Co	Cu	Bi	Sn	0	0.05	0.5	0.69
	Nb	Ti	Fe	Fe	Sb	Bi	0.15	0	0.05	0.65
	Zr	Zr	Ni	Cu	Bi	Sn	0	0.05	0.5	0.61
SISSO+NN+XGB+RF	Ta	Ca	Fe	Fe	Sb	Sb	0.15	0	0	0.68
	Zr	Li	Co	Zn	Bi	Sn	0.3	0.05	0.2	0.65
	Nb	Ca	Fe	Fe	Sb	Sb	0.15	0	0	0.63
	Zr	Zr	Ni	Cu	Bi	Sn	0	0.05	0.5	0.6

zation of predicted materials before their bulk syntheses are attempted. This can help close the time gap between high-throughput screening and experimental validation. Furthermore, we propose an active learning strategy where compositions showing large discrepancies in predicted and experimental zT values are re-included in the dataset and the models retrained. The process will be repeated until the models converge i.e. until the predicted values approximate the true zT value of any given composition. The active learning strategy is especially effective in overcoming data limitations in materials science, where generating experimental data is both costly as well as time-consuming⁶⁴. By iteratively selecting the most probable important data points for the desired property, this strategy can minimize the experimental workload whilst enriching the dataset and improving the prediction accuracy. Therefore, a combination of active learning approach with TFML for experimental validation - which will be the part of our forthcoming work - may render our machine learning workflow a powerful tool for accelerated discovery of hH (TE) materials.

Conclusion

In this work, we have presented a comprehensive and robust machine learning workflow specifically tailored for the discovery of high-performance half-Heusler (hH) thermoelectric materials. We have established a framework to improve ML model generalizability by addressing dataset handling and feature filtering, recognizing that true generalizability involves complexities that conventional loss function optimization cannot capture alone. Our study introduced a novel PCA-based train/test splitting method that ensures an unbiased representation of the chemical space, providing a more accurate gauge of a model’s ability to generalize to unseen materials. Furthermore, the integration of Bayesian hyperparameter optimization with a k-best feature selection strategy allowed us to perform a rigorous and unbiased feature selection for Random Forest, XGBoost, and Neural Networks to predict the complex figure of merit, zT . The “white-box” Sure Independent Screening-Sparsifying Operator (SISSO) method, with a variable search feature filtering, was used for comparison. By employing SHAP (SHapley Additive exPlanations) on RF, XGB, and NN models and interpreting the SISSO descriptors, Temperature (T) was unanimously, but unsurprisingly, identified as the most critical driver of zT , though its relationship was found to be highly context-dependent and non-linear in neural network models. The A-site dopant concentration ($x_{A'}$) and the Heat of Vaporization (HV_A) emerged as the most important features, highlighting the vital role of A-site for TE performance of hH materials. The high-throughput screening (HTS), with ensemble averaging, over a vast and chemically realistic compositional space, using OQMD and Materials Project databases, identified several promising, never-before-studied hH compositions for future DFT and experimental validation. Ultimately, by leveraging the combination of thin-film material libraries (TFML) and active learning strategies for experimental validation, this workflow can serve as a powerful tool for accelerating the development of efficient TE materials, providing a scalable solution to overcome the data limitations inherent in thermoelectrics.

Data availability

The data supporting this article have been included as part of the Supplementary Information. The raw data is available at <https://src.koda.cnrs.fr/icgm-thermoelectrics-ml>. Additional data will be made available upon request.

References

- (1) Goldsmid, H. J. *Introduction to Thermoelectricity*; Berlin, Heidelberg Springer Berlin Heidelberg, 2016.
- (2) Athar, S.; Bergonzoni, A.; Guazzagalloppa, J.; Huillet, C.; Jund, P. Ab Initio and Experimental Investigation of Thermoelectric Properties in a Silica-Based Superinsulating Material. *Journal of physical chemistry. C./Journal of physical chemistry. C* **2023**, *127*, 9973–9980.
- (3) Athar, S.; Guazzagalloppa, J.; Boyrie, F.; Huillet, C.; Jund, P. Carbogels for sustainable and scalable thermoelectric applications. *npj Clean Energy* **2025**, *1*.
- (4) Na, G. S.; Chang, H. A public database of thermoelectric materials and system-identified material representation for data-driven discovery. *npj Computational Materials* **2022**, *8*, 1–11.
- (5) Katsura, Y.; Kumagai, M.; Kodani, T.; Kaneshige, M.; Ando, Y.; Gunji, S.; Imai, Y.; Ouchi, H.; Tobita, K.; Kimura, K.; Tsuda, K. Data-driven analysis of electron relaxation times in PbTe-type thermoelectric materials. *Science and Technology of Advanced Materials* **2019**, *20*, 511–520.
- (6) Athar, S.; Jund, P. Beyond Predicted ZT: Machine Learning Strategies for the Experimental Discovery of Thermoelectric Materials. 2026; <https://arxiv.org/abs/2601.06571>.

(7) Wang, X.; Sheng, Y.; Ning, J.; Xi, J.; Xi, L.; Qiu, D.; Yang, J.; Ke, X. A Critical Review of Machine Learning Techniques on Thermoelectric Materials. *The Journal of Physical Chemistry Letters* **2023**, *14*, 1808–1822.

(8) Na, G. S.; Jang, S.; Chang, H. Predicting thermoelectric properties from chemical formula with explicitly identifying dopant effects. *npj Computational Materials* **2021**, *7*.

(9) Athar, S.; Mecibah, A.; Jund, P. Tackling dataset curation challenges towards reliable machine learning: a case study on thermoelectric materials. *Materials Today Physics* **2025**, *59*, 101948.

(10) Parse, N.; Recatala-Gomez, J.; Zhu, R.; Low, A. K.; Hippalgaonkar, K.; Mato, T.; Katsura, Y.; Pinitsoontorn, S. Predicting High-Performance Thermoelectric Materials With StarryData2. *Advanced Theory and Simulations* **2024**, *7*.

(11) Li, Y.; Zhang, J.; Zhang, K.; Zhao, M.; Hu, K.; Lin, X. Large Data Set-Driven Machine Learning Models for Accurate Prediction of the Thermoelectric Figure of Merit. *ACS Applied Materials & Interfaces* **2022**, *14*, 55517–55527.

(12) Li, W.; Liu, M. Interpretable Machine Learning Workflow for Evaluating and Analyzing the Performance of High-Entropy GeTe-Based Thermoelectric Materials. *ACS Applied Electronic Materials* **2023**, *5*, 4523–4533.

(13) Jia, X.; Aziz, A.; Hashimoto, Y.; Li, H. Dealing with the big data challenges in AI for thermoelectric materials. *Science China Materials* **2024**, *67*, 1173–1182.

(14) Barua, N. K.; Lee, S.; Oliynyk, A. O.; Kleinke, H. Thermoelectric Material Performance (zT) Predictions with Machine Learning. *ACS Applied Materials & Interfaces* **2024**, *17*, 1662–1673.

(15) Abu-Mostafa, Y. S.; Magdon-Ismail, M.; Lin, H.-T. *Learning from data : a short course*; Aml Book: Pasadena, Ca, 2012.

(16) Tranås, R.; Løvvik, O. M.; Tomic, O.; Berland, K. Lattice thermal conductivity of half-Heuslers with density functional theory and machine learning: Enhancing predictivity by active sampling with principal component analysis. *Computational Materials Science* **2021**, *202*, 110938–110938.

(17) Barua, N. K.; Lee, S.; Oliynyk, A. O.; Kleinke, H. Recent strides in artificial intelligence for predicting thermoelectric properties and materials discovery. *Journal of Physics Energy* **2025**,

(18) Nagarajan, G.; Babu, L. D. D. A hybrid feature selection model based on improved squirrel search algorithm and rank aggregation using fuzzy techniques for biomedical data classification. *Network Modeling Analysis in Health Informatics and Bioinformatics* **2021**, *10*.

(19) Gu, Q.; Li, Z.; Han, J. Generalized Fisher score for feature selection. Proceedings of the Twenty-Seventh Conference on Uncertainty in Artificial Intelligence. Arlington, Virginia, USA, 2011; p 266–273.

(20) Deprez, M.; Robinson, E. C. In *Machine Learning for Biomedical Applications*; Deprez, M., Robinson, E. C., Eds.; Academic Press, 2024; pp 175–192.

(21) Biswas, S.; Bordoloi, M.; Purkayastha, B. Review on Feature Selection and Classification using Neuro-Fuzzy Approaches. *International Journal of Applied Evolutionary Computation* **2016**, *7*, 28–44.

(22) Guyon, I.; Weston, J.; Barnhill, S.; Vapnik, V. Gene Selection for Cancer Classification Using Support Vector Machines. *Machine Learning* **2002**, *46*, 389–422.

(23) Bhattacharjee, D.; Kundavu, K.; Saraswat, D.; Raghuvanshi, P. R.; Bhattacharya, A. Thorough Descriptor Search to Machine Learn the Lattice Thermal Conductivity of Half-Heusler Compounds. *ACS Applied Energy Materials* **2022**, *5*, 8913–8922.

(24) Breiman, L. Random Forests. *Machine Learning* **2001**, *45*, 5–32.

(25) Chen, T.; Guestrin, C. XGBoost: A Scalable Tree Boosting System. Proceedings of the 22nd ACM SIGKDD International Conference on Knowledge Discovery and Data Mining (KDD '16). New York, NY, USA, 2016; pp 785–794.

(26) Kabir, H. M. D.; Abdar, M.; Jalali, S. M. J.; Khosravi, A.; Atiya, A. F.; Nahavandi, S. SpinalNet: Deep Neural Network with Gradual Input. *arXiv preprint arXiv:2007.03347* **2020**,

(27) Ouyang, R.; Curtarolo, S.; Ahmetcik, E.; Scheffler, M.; Ghiringhelli, L. M. SISSO: A compressed-sensing method for identifying the best low-dimensional descriptor in an immensity of offered candidates. *Phys. Rev. Mater.* **2018**, *2*, 083802.

(28) Anand, S.; Wood, M.; Xia, Y.; Wolverton, C.; Snyder, J. Double Half-Heuslers. *SSRN Electronic Journal* **2019**,

(29) Mentel, L. mendeleev - A Python package with properties of chemical elements, ions, isotopes and methods to manipulate and visualize periodic table. 2021; <https://github.com/lmmmentel/mendeleev>.

(30) van der Maaten, L.; Hinton, G. Visualizing Data using t-SNE. *Journal of Machine Learning Research* **2008**, *9*, 2579–2605.

(31) Goodfellow, I.; Bengio, Y.; Courville, A. *Deep Learning*; MIT Press: Cambridge, MA, 2016.

(32) Pearson, K. Note on regression and inheritance in the case of two parents. *Proceedings of the Royal Society of London* **1895**, *58*, 240–242.

(33) Bron, C.; Kerbosch, J. Algorithm 457: Finding All Cliques of an Undirected Graph. *Communications of the ACM* **1973**, *16*, 575–577.

(34) Guo, Z.; Hu, S.; Han, Z.-K.; Ouyang, R. Improving Symbolic Regression for Predicting Materials Properties with Iterative Variable Selection. *Journal of Chemical Theory and Computation* **2022**, *18*, 4945–4951, PMID: 35834781.

(35) Saal, J. E.; Kirklin, S.; Aykol, M.; Meredig, B.; Wolverton, C. Materials Design and Discovery with High-Throughput Density Functional Theory: The Open Quantum Materials Database (OQMD). *JOM* **2013**, *65*, 1501–1509.

(36) Jain, A.; Ong, S. P.; Hautier, G.; Chen, W.; Richards, W. D.; Dacek, S.; Cholia, S.; Gunter, D.; Skinner, D.; Ceder, G.; Persson, K. A. Commentary: The Materials Project: A materials genome approach to accelerating materials innovation. *APL Materials* **2013**, *1*, 011002.

(37) Xie, W.; Weidenkaff, A.; Tang, X.; Zhang, Q.; Poon, J.; Tritt, T. Recent Advances in Nanostructured Thermoelectric Half-Heusler Compounds. *Nanomaterials* **2012**, *2*, 379–412.

(38) Bergstra, J.; Bardenet, R.; Bengio, Y.; Kégl, B. Algorithms for Hyper-Parameter Optimization. Advances in Neural Information Processing Systems (NeurIPS). 2011; pp 2546–2554.

(39) Bergstra, J.; Yamins, D.; Cox, D. D. Making a Science of Model Search: Hyperparameter Optimization in Hundreds of Dimensions for Vision Architectures. Proceedings of the 30th International Conference on Machine Learning (ICML). 2013; pp 115–123.

(40) Zhong, Y.; Hu, X.; Sarker, D.; Su, X.; Xia, Q.; Xu, L.; Yang, C.; Tang, X.; Levchenko, S. V.; Han, Z.; Cui, J. Data analytics accelerates the experimental discovery of Cu_{1-x}Ag_xGaTe₂ based thermoelectric chalcogenides with high figure of merit. *J. Mater. Chem. A* **2023**, *11*, 18651–18659.

(41) Wang, H. et al. International Round-Robin Study of the Thermoelectric Transport Properties of an n-Type Half-Heusler Compound from 300 K to 773 K. *Journal of Electronic Materials* **2015**, *44*, 4482–4491.

(42) Bhadeshia, H. K. D. H.; Dimitriu, R. C.; Forsik, S.; Pak, J. H.; Ryu, J. H. Performance of neural networks in materials science. *Materials Science and Technology* **2009**, *25*, 504–510.

(43) Farhadi, Z.; Bevrani, H.; Feizi-Derakhshi, M.-R. Combining Regularization and Dropout Techniques for Deep Convolutional Neural Network. Global Energy Conference (GEC), Batman, Turkey, 2022. 2022; p 335–339.

(44) Dou, B.; Zhu, Z.; Merkurjev, E.; Lu, K.; Chen, L.; Jian, J.; Zhu, Y.; Liu, J.; Zhang, B.; Wei, G.-W. Machine Learning Methods for Small Data Challenges in Molecular Science. *Chemical Reviews* **2023**, *123*, 8736–8780.

(45) Kondratyuk, D.; Tan, M.; Brown, M.; Gong, B. When Ensembling Smaller Models is More Efficient than Single Large Models. *arXiv (Cornell University)* **2020**,

(46) Zhu, H. et al. Discovery of TaFeSb-based half-Heuslers with high thermoelectric performance. *Nature Communications* **2019**, *10*.

(47) Zhou, M.; Chen, L.; Feng, C.; Wang, D.; Li, J.-F. Moderate-temperature thermoelectric properties of TiCoSb-based half-Heusler compounds $Ti_{1-x}TaxCoSb$. *Journal of Applied Physics* **2007**, *101*.

(48) Mohamed, M.; Ibrahim, E.; Rodriguez, N.; Hampel, S.; Büchner, B.; Schierning, G.; Nielsch, K.; He, R. Tuning of the electronic and phononic properties of NbFeSb half-Heusler compound by Sn/Hf co-doping. *Acta Materialia* **2020**, *196*, 669–676.

(49) Zhu, H. et al. Discovery of ZrCoBi based half Heuslers with high thermoelectric conversion efficiency. *Nature Communications* **2018**, *9*.

(50) Kim, S. W.; Kimura, Y.; Mishima, Y. High temperature thermoelectric properties of TiNiSn-based half-Heusler compounds. *Intermetallics* **2007**, *15*, 349–356.

(51) Gong, B.; Liu, F.; Zhu, J.; Wang, X.; Ao, W.; Zhang, C.; Li, Y.; Li, J.; Xie, H. Effects of Sc, Ti, Hf, V, Nb and Ta doping on the properties of ZrNiSn alloys. *Journal of Materials Science* **2019**, *54*, 10325–10334.

(52) Heremans, J. P.; Jovovic, V.; Toberer, E. S.; Saramat, A.; Kurosaki, K.; Charoenphakdee, A.; Yamanaka, S.; Snyder, G. J. Enhancement of Thermoelectric Efficiency in PbTe by Distortion of the Electronic Density of States. *Science* **2008**, *321*, 554–557.

(53) Zhu, H.; Wang, G.; Wang, G.; Zhou, X.; Lu, X. The role of electronic affinity for dopants in thermoelectric transport properties of InTe. *Journal of Alloys and Compounds* **2021**, *869*, 159224–159224.

(54) Kim, Y.-J.; Tan, Y.-F.; Kim, S. Two-dimensional lattice Boltzmann modeling for effective thermal conductivity in carbon black filled composites. *Journal of composite materials* **2017**, *52*, 2047–2053.

(55) Eivari, H. A.; Sohbatzadeh, Z.; Mele, P.; Assadi, N. Low thermal conductivity: fundamentals and theoretical aspects in thermoelectric applications. *Materials Today Energy* **2021**, *21*, 100744–100744.

(56) Gurunathan, R.; Hanus, R.; Dylla, M.; Katre, A.; Snyder, G. J. Analytical Models of Phonon–Point-Defect Scattering. *Physical Review Applied* **2020**, *13*.

(57) Quinn, R. J.; Bos, J.-W. G. Advances in half-Heusler alloys for thermoelectric power generation. *Mater. Adv.* **2021**, *2*, 6246–6266.

(58) Ando, Y.; Miyamoto, N.; Segawa, K.; Kawata, T.; Terasaki, I. Specific-heat evidence for strong electron correlations in the thermoelectric material(Na,Ca)Co₂. *Physical review. B, Condensed matter* **1999**, *60*, 10580–10583.

(59) Cui, T.; Xuan, Y.; Yin, E.; Li, Q.; Li, D. Experimental investigation on potential of a concentrated photovoltaic-thermoelectric system with phase change materials. *Energy* **2017**, *122*, 94–102.

(60) Liang, Z.; Shang, H.; Xu, C.; Shi, X.; Zhang, F.; Ren, W.; Song, S.; Ding, F.; Ren, Z. New insights into the effect of chemical bonding strength on thermoelectric performance and stability in YbMg₂Bi₂ toward practical thermoelectric applications. *Materials Today Physics* **2022**, *28*, 100858–100858.

(61) Lundberg, S. M.; Lee, S.-I. A unified approach to interpreting model predictions. Proceedings of the 31st International Conference on Neural Information Processing Systems. Red Hook, NY, USA, 2017; p 4768–4777.

(62) Naftaly, U.; Intrator, N.; Horn, D. Optimal ensemble averaging of neural networks. *Network: Computation in Neural Systems* **1997**, *8*, 283–296.

(63) Talley, K. R.; Sherbondy, R.; Zakutayev, A.; Brennecka, G. L. Review of high-throughput approaches to search for piezoelectric nitrides. *Journal of vacuum science & technology* **2019**, *37*, 060803–060803.

(64) Kusne, A. G. et al. On-the-fly closed-loop materials discovery via Bayesian active learning. *Nature Communications* **2020**, *11*.

Acknowledgement

We acknowledge the financial support from the Agence Nationale de la Recherche (ANR), France under the ANR-DFG project CombiHeusler (ANR-24-CE92-0053-01).

Author Contribution declaration

S.A.: Writing—Original draft preparation, Visualization, Methodology, Investigation, Data curation, Conceptualization; A.M.: Writing—Original draft preparation, Visualization, Methodology, Investigation, Data curation; P.J.: Conceptualization, Supervision, Writing-Reviewing and Editing, Validation

Competing Interest declaration

The authors declare no competing interests.